

Topological Hall Effect and Skyrmion-like Bubbles at a Charge-transfer Interface

*Zhi Shiuh Lim, Changjian Li, Zhen Huang, Xiao Chi, Jun Zhou, Shengwei Zeng, Ganesh Ji Omar, Yuan Ping Feng, Andriyo Rusydi, Stephen John Pennycook, Thirumalai Venkatesan, Ariando Ariando**

Dr. Z. S. Lim, Dr. C. Li, Dr. Z. Huang, Dr. S.W. Zeng, G. J. Omar, Prof. T. Venkatesan, Assoc. Prof. A. Ariando
NUSNNI-NanoCore, National University of Singapore, Singapore 117411
email: ariando@nus.edu.sg

Dr. Z. S. Lim, Dr. Z. Huang, Dr. X. Chi, Dr. J. Zhou, Dr. S.W. Zeng, G. J. Omar, Prof. Y. P. Feng, Prof. T. Venkatesan, Assoc. Prof. A. Rusydi, Assoc. Prof. A. Ariando
Department of Physics, National University of Singapore, Singapore 117542

Dr. X. Chi, Assoc. Prof. A. Rusydi
Singapore Synchrotron Light Source (SSLS), National University of Singapore, 5 Research Link, Singapore 117603

Dr. C. Li, Prof. S. J. Pennycook, Prof. T. Venkatesan
Department of Materials Science and Engineering, National University of Singapore, Singapore 117575

Keywords: Charge transfer, Spin-orbit coupling, Topological Hall Effect, CaIrO_3 , Skyrmion-like bubbles

Abstract:

Exploring exotic interface magnetism due to charge transfer and strong spin-orbit coupling has profound application in future development of spintronic memory. Here, the emergence, tuning and interpretation of hump-shape Hall Effect from a $\text{CaMnO}_3/\text{CaIrO}_3/\text{CaMnO}_3$ trilayer structure are studied in detail. The hump signal can be recognized as Topological Hall Effect suggesting the presence of Skyrmion-like magnetic bubbles; but the debated alternative interpretation where the signal being an artefact between two cancelling Anomalous Hall Effect loops is also discussed. Firstly, by tilting the magnetic field direction, the evolution of Hall signal suggests transformation of the bubbles' topology into a more trivial kind. Secondly, by varying the thickness of CaMnO_3 , the optimal thicknesses for the hump signal emergence are found, suggesting a tuning of charge transfer fraction. Using high-resolution transmission electron microscopy, a stacking fault is also identified, which distinguishes the top and bottom $\text{CaMnO}_3/\text{CaIrO}_3$ interfaces in terms of charge transfer fraction and possible interfacial Dzyaloshinskii-Moriya Interaction. Finally, a spin-transfer torque experiment revealed a low threshold current density of $\sim 10^9 \text{ A/m}^2$ for initiating the bubbles' motion. This discovery opens a possible route for integrating Skyrmions with antiferromagnetic spintronics.

The key advantages to be offered by the antiferromagnetic spintronics field are storing information with immunity to external magnetic field perturbation, and ultrafast (\sim THz) switching dynamics^[1]. Recently, this field sparked worldwide research interest when reliable all-electrical manipulation (via spin-orbit torque (SOT)) and detection (via anisotropic magnetoresistance (AMR)) of antiferromagnetic states was achieved in CuMnAs^[2]. On the other hand, the abundant ferromagnetic Skyrmions currently known are promising candidates as information-storing bits in the proposed “racetrack memory” design^[3]. Skyrmion racetrack memories^[4] are expected to operate at ultralow current density^[5, 6] and thus energy saving due to Skyrmions’ intrinsic ability to evade defects-pinning^[7]. Among the efforts in building such realistic devices, a few crucial challenges must be overcome: Firstly, Skyrmions should be robustly nucleated or deleted at the WRITE-head by a localized current injection^[8], or more preferably by a current-less electric field tuning of the magnetic energy landscape^[9]. Secondly, when moving driven by current, the Skyrmion Hall Effect (SkHE)^[10, 11] is detrimental because the transverse deflection would lead to their annihilation at sidewalls especially at high speed. Several strategies for suppressing the gyromagnetic Magnus force have emerged, namely by stabilizing Skyrmions in ferrimagnetic materials^[12] or synthetic antiferromagnetic multilayers coupled by Ruderman–Kittel–Kasuya–Yosida (RKKY) interaction^[13], albeit an actual antiferromagnetic Skyrmion remains elusive. Thirdly, Skyrmions detection at the READ-head should be performed by a compact Tunnelling Non-collinear Magnetoresistance (TNcMR)^[14] mechanism. Notably, the first and second aspects mentioned above pose some contradictions, i.e.: a metallic racetrack is required for current-driven Skyrmions motion, yet electric field gating for Skyrmions nucleation would require an insulator with low carrier density to be effective. To bridge this gap, researchers would turn attention to multifunctional oxide heterostructures in search of compromising properties.

In perovskite oxides, studies on charge-transfer driven interfacial physics have grown equally fruitful. The “polar-discontinuous” combinations (e.g. $\text{LaAlO}_3/\text{SrTiO}_3$) yielded confined high-mobility two-dimensional electron gas (2DEG) with magnetism and even superconductivity^[15]. Whereas in nonpolar combinations, the driving force of charge transfer has been understood by an initial O2p band alignment before contact and follows the trend of energy gap between O2p and valence band ($E_{\text{O2p}}-E_{\text{F}}$)^[16]; which is distinct from the early Schottky-Mott rule^[17] emphasizing work-function difference. Consistent to this concept, charge transfer from Ir^{4+} to Mn^{4+} has been experimentally verified in $\text{SrMnO}_3/\text{SrIrO}_3$ superlattices^[18], and yielded interface ferromagnetism, perpendicular magnetic anisotropy (PMA) and Anomalous Hall Effect (AHE). Besides, owing to the strong spin-orbit coupling (SOC) contributed by SrIrO_3 , Neel-type Skyrmion is also predicted to exist in $\text{La}_{1-x}\text{Sr}_x\text{MnO}_3/\text{SrIrO}_3$ superlattice by a Monte-Carlo simulation^[19], which is very valuable since such system is semiconducting and removes the contradiction mentioned above. In this work, we attempt to reduce the complexity of superlattice into a trilayer structure of $\text{CaMnO}_3(3\text{uc})/\text{CaIrO}_3(19\text{uc})/\text{CaMnO}_3(3\text{uc})$, abbreviated as $\text{Ca-Mb}_3\text{I}_{19}\text{Mt}_3$. In addition to AHE, we also observe the emergence of hump-shape Hall features in temperature range of 10-50 K (**Figure 1c**) that resembles Topological Hall Effect (THE), suggesting presence of Skyrmion-like bubbles. By various examinations such as tilting magnetic field direction, tuning CaMnO_3 thicknesses (Mb and Mt), atomic survey and current-driven dynamics, our experimental results shall present valuable insights to the community.

Results:

The mechanism of THE is well-understood – as conduction electrons hopping across non-coplanar magnetic textures, strong Hund’s coupling (J_{H}) between the electrons’ spin ($\hat{\mathbf{S}}$) and the gradually varying local moment ($\hat{\mathbf{m}}$) causes the electrons to gain a real-space Berry phase, leading to transverse deflection^[20, 21]. This effect requires a net topological charge

$$Q = \frac{1}{4\pi} \sum_{ijk} 2 \tan^{-1} \frac{\hat{\mathbf{m}}_k \cdot (\hat{\mathbf{m}}_i \times \hat{\mathbf{m}}_j)}{1 + \hat{\mathbf{m}}_i \cdot \hat{\mathbf{m}}_j + \hat{\mathbf{m}}_j \cdot \hat{\mathbf{m}}_k + \hat{\mathbf{m}}_k \cdot \hat{\mathbf{m}}_i} \text{ among triads of local moments or equivalently}$$

$$Q = \frac{1}{4\pi} \int \hat{\mathbf{m}} \cdot \left(\frac{\partial \hat{\mathbf{m}}}{\partial x} \times \frac{\partial \hat{\mathbf{m}}}{\partial y} \right) dx dy, \text{ and has been observed in manganites}^{[21, 22]}, \text{ B20 compounds}^{[23]},$$

pyrochlore frustrated antiferromagnets^[24], ultrathin SrRuO₃ systems^[25, 26], and topological insulators^[26-28]. Since it is well-known that a typical magnetic phase evolution involves stripe-domains at zero-field, Skyrmions at intermediate regime, and collinear ferromagnet at large field, $\rho_{\text{THE}}(H)$ is expected to adopt a hump-shape^[26, 29]. While the hysteretic saturated collinear ferromagnetic background of where Skyrmions are embedded will contribute a square $\rho_{\text{AHE}}(H)$ loop. This is the “AHE+THE” picture.

However, in recognition of the recent debates^[30], we caution that the data in Figure 1c can also be interpreted as a partial cancellation between two AHE loops with opposite signs and different coercive fields (H_c), which can be simulated by two pairs of Langevin functions:

$$\mathcal{L}_{12}(H) = A_{12} \left\{ \coth \left[\frac{g\mu_0\mu_B J_{12}}{k_B T} (H \pm H_{c1,2}) \right] - \frac{k_B T}{g\mu_0\mu_B J_{12} (H \pm H_{c1,2})} \right\} \text{ (Figure S1a). We can infer the}$$

non-equivalent top and bottom CMO/CIO interfaces to be the possible sources of opposite-sign AHE loops, such that the hump emergence only hosts trivial collinear domains instead of Skyrmions-like bubbles. To clarify the superexchange mechanism in Mn⁴⁺/Ir⁴⁺ combination, we show a sketch of single-ion density-of-states (DOS) to illustrate the two possible charge transfer pathways into the e_g^\uparrow and t_{2g}^\downarrow bands of Mn⁴⁺ that are in proximity in energy (**Figure 1a**). Both the Ir5d_{J_{eff}=1/2} – O2p_{x,y} – Mn3d_{xz,yz} (π - π) and Ir5d_{J_{eff}=1/2} – O2p_{x,y} – Mn3d_{3z²-r²} (π - σ) transfer pathways are viable (**Figure 1b**), the former is expected to be weak due to low orbital overlap while the latter is enabled by octahedral tilt. This proximity is known from O K edges of X-ray absorption (XAS) in bulk CaMnO₃ as a huge peak at ~528.8 eV^[31]. Several *ab-initio* calculations indicated that the Mn e_g^\uparrow orbital is dominantly filled after charge transfer^[32, 33], consistent to our XAS result (**Figure S2b**) suggesting that e_g^\uparrow is slightly

lower than t_{2g}^\downarrow . This results in a ferromagnetic Mn-O-Mn double-exchange along xy-plane via the $d_{x^2-y^2}$ orbitals, but an antiparallel Ir-O-Mn superexchange involving the $d_{xz,yz}$ and $d_{3z^2-r^2}$ orbitals along z-direction. Considering the larger density-of-states ($DOS(E_F)$) due to heavier effective masses in t_{2g} bands compared to e_g , we expect the spin-polarization, $P_s = \frac{DOS_\uparrow(E_F) - DOS_\downarrow(E_F)}{DOS_\uparrow(E_F) + DOS_\downarrow(E_F)} < 0$, leading to a negative-sign ρ_{AHE} loop (**Figure 1d**, top). This can be understood from the semiclassical intrinsic transverse velocity^[34]: $v_{i\perp,\uparrow\downarrow}(\mathbf{k}) = \mp \frac{e}{\hbar} \mathbf{E}_\parallel \times \boldsymbol{\Omega}_{i,z}(\mathbf{k})$ where $\boldsymbol{\Omega}_i(\mathbf{k}) = \nabla_{\mathbf{k}} \times \langle u_i(\mathbf{k}) | \nabla_{\mathbf{k}} | u_i(\mathbf{k}) \rangle$ is the k-space Berry curvature at the i -th band and \mathbf{E}_\parallel is the linear electric field. Hence, the AHE current density is $\mathbf{j}_\perp = -e \sum_{i,\uparrow\downarrow} \int_{BZ} \frac{d^3k}{(2\pi)^3} f_D(E(k)) v_{i\perp,\uparrow\downarrow}(k) \approx P_s \frac{ne^2}{\hbar} [\mathbf{E}_\parallel \times \langle \boldsymbol{\Omega}_z \rangle]$, where n , f_D and $\langle \dots \rangle$ are total carrier density, Fermi-Dirac distribution and average. Note that such picture of negative-sign ρ_{AHE} loop and antiparallel M_{Mn} - M_{Ir} moments alignment agree well with J. Nichols' result^[18] and our first-principle calculation on superlattice (**Figure S4c**). Conversely, if the charge-transfer fraction is reduced, lowering E_F and shut the t_{2g}^\downarrow conduction channel, we expect $P_s > 0$ (**Figure 1d**, bottom), together with the suppression of xy-plane ferromagnetic Mn-O-Mn into canted antiferromagnetic. Such magnetic phase evolution has been understood via a Hamiltonian $\tilde{\mathcal{H}} = -t \cos\left(\frac{\beta}{2}\right) \sum_{\langle ij \rangle} (a_{i\uparrow}^\dagger a_{j\uparrow} + \text{h.c.}) + \sum_{\langle ij \rangle} J_{ex} (\hat{\mathbf{m}}_i \cdot \hat{\mathbf{m}}_j)$, which simplifies into an energy equation $E = -4x|t| \cos\left(\frac{\beta}{2}\right) + J_{ex} \cos(\beta)$ to be minimized, where t , β , J_{ex} and x are the hopping integral, angle deviating from ferromagnetic alignment, superexchange coupling and charge-transfer fraction respectively^[33]. For CaMnO_3 featuring larger octahedral tilts (smaller t) and stronger J_{ex} than that of SrMnO_3 , a higher critical charge-transfer fraction ($x_c = \frac{2J_{ex}}{|t|}$) is required to achieve the ideal ferromagnetic alignment^[33]. In turn, the $P_s > 0$ scenario when $M_{Mn, \text{canted}} > |M_{Ir}|$ would then be more likely to occur, although it has been

neglected thus far. In short, we recognize here that the “Bi-AHE” scenario, represented by the negative-sign \mathcal{L}_2 and positive-sign \mathcal{L}_1 , cannot be ruled out.

In the magnetization-temperature (M - T) curves (**Figure 2a**), there are interestingly three obvious kinks indicating magnetic phase transitions. We ascribe the lowest $T_1 \sim 65$ K to the T_N of antiferromagnetic $\text{Mn}^{4+}\text{-O}^{2-}\text{-Mn}^{4+}$ superexchange, which is ubiquitous in both in-plane and out-of-plane fields. The intermediate $T_2 \sim 105$ K is the T_C of $\text{Mn}^{(4-\delta)+}\text{-O}^{2-}\text{-Ir}^{(4+\delta)+}$ superexchange with PMA since it only exists at $H \parallel [001]$; while the highest $T_3 \sim 185$ K could be the onset of Ir^{4+} spin nematic/liquid order^[35] due to its proximity with Mn^{4+} near the interfaces. Besides, the magnetization-field (M - H) loops (**Figure 2b**) are almost temperature independent and very narrow, not showing H_c comparable to that of AHE loops; and correspondingly the magnetoresistance (MR) in **Figure 2f** are negative parabolic but hysteretic “butterfly loops” are absent. Putting aside the humps, the presence of strong AHE signal but small saturation-magnetization (M_{sat}) implies a dominant antiferromagnetic Mn^{4+} in CMO, while the narrow H_c could originate from the magnetized Ir^{4+} moments in proximity to Mn^{4+} . The z-component of enhanced interfacial $\text{Mn}^{(4-\delta)+}$ canted moment due to the charge transfer is almost undetectable in magnetometry but is available to break time-reversal symmetry (TRS) and contribute a net Berry curvature.

To shed light on the anisotropic magneto-transport, we further performed rotation of magnetic field as illustrated in **Figure 2c**. The linear magnetoresistance (AMR) (**Figure 2f-g**) suggests a trend of anisotropy $K_{[011]} < K_{[001]} < K_{[010]}$ in a sequence of increasingly easier magnetic axis (see supporting information). More insights emerge when such rotation configuration is applied on Hall Effect measurement (**Figure 2d-e**). At 30 K and $H \parallel [001]$, the extraordinary part of Hall Effect $\rho_{xy}\text{-}R_o B$ can be decomposed following either the “AHE+hump” or the “Bi-AHE” schemes. Details of fittings are given in Figure S1a, and we can perceive that the magnitudes of \mathcal{L}_2 and hump are proportional. As shown in **Figure 2d**,

the net AHE is seen to increase concomitantly with the diminishing of humps within the range of $30^\circ < \theta < 60^\circ$; conversely, \mathcal{L}_1 stays constant although \mathcal{L}_2 starts diminishing at $\theta > 30^\circ$. Both the net AHE and \mathcal{L}_1 then vanish fast above $\theta > 60^\circ$ because eventually the Hall Effect cannot be measured with an in-plane field. To understand the rising net AHE after $\theta > 30^\circ$, we draw analogy to the topology transformation once observed in several dipolar- (demagnetization) stabilized bubble systems, namely: (Sc,Mg)-doped $\text{Ba}_3\text{Fe}_{12}\text{O}_{19}$ ^[36] and $\text{La}_{0.825}\text{Sr}_{0.175}\text{MnO}_3$ ^[37]. In those systems, stripe domains dominated at zero-field as usual, while Bloch-type Skyrmions ($Q=1$) with mixed clockwise and counterclockwise helicities ($Q_h = \pm\pi/2$)^[38] existed at small magnetic fields of $\sim 0.1\text{-}0.2$ T. Upon tilting the field towards in-plane direction, Bloch-type Skyrmions are transformed into the “type-II” bubbles with $Q=0$ since they are just made of two counter-propagating Bloch lines. This transformation event may suppress THE and enhance AHE, since the type-II bubbles are equivalent to stripe domains. It is also reasonable from Ginzburg-Landau framework^[39], where three in-plane helical magnons with mutual 120° wave-vectors in superposition would create a triangular Skyrmion-lattice at small out-of-plane field, but an in-plane field would disturb their balance, transforming Skyrmions back into stripes. Correspondingly in **Figure 2e**, both $H_{c,\text{AHE}}$ and H_{c1} increase following the $\sim 1/\cos(\theta)$ trend, yet the hump peak field (H_{hp}) and H_{c2} remain constant with θ up to their abrupt disappearance at $\theta=60^\circ$. This shows a stark difference between the net AHE (\mathcal{L}_1) and hump (\mathcal{L}_2) in terms of their anisotropy and origin.

Next, we investigate into thickness dependence of the Hall components, presented in the “AHE+hump” format since its fitting and decomposition are more straightforward. First, assisted by topography surveys (**Figure 3a**), we are confident that the CMO film growth mode is in layer-by-layer with minimal roughness, while the CIO is in Stranski-Krastanov growth mode with tendency to roughen at large thickness, and 19uc is within the acceptable thickness range. In **Figure 3b** (left panel), removing the top CMO ($\text{Ca-Mb}_3\text{I}_{19}\text{Mt}_0$) retains the

AHE (with Anomalous Hall angle $\Theta_{\text{AH}} \sim 0.00145$), yet suppresses the humps. If following the “AHE+THE” interpretation, we may assume that the top CMO/CIO interface contributes a Dyzalooshinskii-Moriya interaction (DMI) for Neel-type Skyrmions; or if following the “Bi-AHE” interpretation via $\mathcal{L}_{1,2}$, we may assign \mathcal{L}_2 for the top interface and \mathcal{L}_1 for the bottom. Either way, such distinction between the two interfaces warrants a detailed atomic survey (**Figure 4**). By tuning the top CMO thickness (M_t) at constant bottom CMO thickness ($M_b=3\text{uc}$) (**Figure 3c**), we observed a relatively constant AHE, yet the hump signal reaches a peak at $M_t \sim 4\text{uc}$. On the other hand, tuning M_b at $M_t=3\text{uc}$ (**Figure 3d**) produced peaks at $M_b \sim 3\text{uc}$ for both the apparent AHE and hump signals. It is possible to explain the absence of hump or \mathcal{L}_2 at the four endpoints. While the reason at regime ① is the absence of the top interface, regime ② (large M_t) can be understood as exceeding the Thomas-Fermi screening length (l_{TF}) of charge transfer, resulting in a lack of confinement and lower charge transfer density below a certain threshold. We may estimate $l_{\text{TF}} = \sqrt{\frac{\epsilon_0 \epsilon_r k_B T}{e^2 n_c}} \sim 8\text{uc}$ at 30 K, approximately agreeing with **Figure 3c**, where $n_c = \left(\frac{1}{4\alpha_0}\right)^3 = \left(\frac{e^2 m_e^*}{16\pi\epsilon_0 \epsilon_r \hbar^2}\right)^3$ from Mott criterion^[40], α_0 is the effective Bohr radius, $\epsilon_r \sim 150$ and $m_e^* \sim 4.3m_0$ for CaMnO_3 ^[41]. On other hand, at large CMO thickness and low charge transfer fraction, it is also reasonable to expect that the criteria of Skyrmion-like bubbles formation are not fulfilled, i.e. either $\frac{D}{\sqrt{J_{\text{ex}} K_u}} < \frac{4}{\pi}$ for DMI-stabilized Skyrmions^[42] due to J_{ex} being too strongly antiferromagnetic, or $\frac{2K_u}{\mu_0 M_{\text{sat}}^2} < 1$ for dipolar-stabilized bubbles^[43] due to lack of strong out-of-plane uniaxial anisotropy K_u . While regime ③ corresponding to $\text{Ca-Mb}_0\text{I}_9\text{Mt}_3$ is trivial: direct deposition of CIO on $\text{LaAlO}_3(001)$ results in island growth mode, severely suppresses the charge transfer at all interfaces and thus all extraordinary Hall components vanish. Lastly at regime ④ (large M_b), the argument of exceeding l_{TF} similar to regime ② is also applicable for the bottom CMO, albeit no roughening occurs.

In **Figure S1b-c**, we show that reducing the CIO thickness in the trilayer structure results in a sign-reversal of the Ordinary Hall Effect (OHE) gradient (R_o) from negative to positive, accompanying a linear enhancement of net AHE. The R_o sign-reversal is not surprising, since the bulk-like CIO in perovskite polymorph is known as a near-compensated semimetal ($n_e=n_h$) with electron and hole pockets residing at different k-points with comparable mobilities^[44]. As shown in **Figure 3e-f**, we fabricated $[\text{CMO}_{m\text{-uc}}+\text{CIO}_{m\text{-uc}}]_{\times 20/m}$ superlattices to validate the competition between $\mathcal{L}_{1,2}$ controlled by charge transfer fraction. Indeed, a clear sign-reversal of ρ_{AHE} loops from $[m=1]\text{-SL}$ (negative) to $[m=2]\text{-SL}$ (positive) is observed down to low temperature. A comparison of the charge-transfer fraction is evidenced from the superlattices' XAS Mn $L_{2,3}$ edges peak shifts, O K edges spectral weight transfer, and ferromagnetic T_c (**Figure S2a-d**). This is consistent to our central concept (Figure 1a) that the reduced charge transfer limited by less interface density per unit volume in $[m=2]\text{-SL}$ would yield a positive-sign ρ_{AHE} loop. Furthermore in $[m=2]\text{-SL}$ and $\text{Ca-Mb}_3\text{I}_{19}\text{Mt}_3$, a thermal excitation at elevated temperature would shift E_F higher and reach the $P_s<0$ conduction channel, resulting in a temperature-driven ρ_{AHE} sign-reversal from positive to negative ($\sim 60\text{-}70\text{ K}$). Yet such temperature-driven sign-reversal is never observed in $[m=1]\text{-SL}$, justifying the argument that e_g^\uparrow has a lower band edge than t_{2g}^\downarrow .

In Figure 4, we gain further insight from distinguish the top and bottom interfaces of $\text{Ca-Mb}_3\text{I}_{19}\text{Mt}_3$ in terms of atomic structures and bond angles, by employing cross-sectional scanning transmission electron microscopy (STEM). As shown in **Figure 4a-b**, while the $\text{LAO}(001)$ substrate has an AO-termination, the bottom CMO adjacent to $\text{LAO}(001)$ is not a perfect ABO_3 perovskite – a stacking fault of two adjacent CaO-CaO planes is found, which resembles a portion of $\text{A}_3\text{B}_2\text{O}_7$ member of the Ruddlesden-Popper series. The regional and randomly distributed nature of such stacking fault is evident by comparing **Figure 4a,c**, but is completely absent in the top CMO. This causes the bottom CIO/CMO interface to have a

mixed termination and more diffuse than the top CMO/CIO interface. Besides, by analysing the atomic positions, the B-O-B bond angle is revealed to become smaller (bent) with increasing distance away from the substrate (**Figure 4d**). This indicates suppression of the films' octahedral tilt by close proximity to the cubic-lattice LAO(001) substrate^[45, 46], and to sign conflict between t_{2g} and e_g orbital wavefunctions^[47]; while the top CMO is unaffected, making a bond angle of $\sim 160^\circ$ consistent to unstrained CMO^[46].

Finally, the Skyrmion dynamics driven by spin-transfer torque (STT) described by the Thiele's equation^[7, 48] forms an important aspect in developing Skyrmion racetrack memories. The dissipative and the Magnus force terms respectively contribute the parallel ($v_{sk,\parallel}$) and transverse ($v_{sk,\perp}$) Skyrmion velocity components. Upon de-pinning with current density exceeding a threshold j_c , Skyrmions in parallel motion to the drift velocity of spin-polarized electrons v_e would suppress the Topological Hall force^[6, 49] by $\mathbf{F}_{THE} = (e/2)(\mathbf{v}_e - \mathbf{v}_{sk}) \cdot \frac{h}{e\pi r_{sk}^2} \hat{\mathbf{z}}$ due to the reducing relative velocity factor. In **Figure 5a**, our Ca-Mb₃I₁₉Mt₃ trilayer produced a clear onset with $j_c \sim 2 \times 10^9$ A/m² ($I \sim 600$ μ A), which is still high compared to the ultralow benchmark of $\sim 10^6$ A/m² set by B20 compounds Bloch-type Skyrmions^[5, 6]. Following methods from Ref. [6], the bubbles' velocity components can be estimated by $v_{sk,\parallel}(J) = -\left|\frac{e}{q_e}\right| \frac{j\Delta\rho_{THE}(J)R_0(j \ll j_c)}{\rho_{THE}(j \ll j_c)}$ and $v_{sk,\perp} = \frac{j_c}{\sqrt{j^2 - j_c^2}} v_{sk,\parallel}$ (**Figure 5b**). Changing the measurement current mode from continuous to a 20-ms pulse-width produces the similar trend of diminishing ρ_{THE} , yet blurs the j_c onset. Such blurring is probably due to repetitive transition of the bubbles' motion between "creep" and "steady-flow" regimes^[10, 50]. Logically, high-current measurement leads to heat dissipation. We expect H_c of AHE be very sensitive to any temperature change; yet **Figure 5a** shows that H_c remains constant at the diminishing ρ_{AHE} and ρ_{THE} . We may relate the rate of temperature change $\frac{\partial T}{\partial t} \sim \frac{j^2 \rho_{xx}}{C_P}$ to thermal power via linear resistivity (ρ_{xx}) and molar heat capacity (C_P). Comparing to typical metallic SOT experiments

of ferromagnets where Joule heating is usually severe, our $\rho_{xx} \sim 10^{-6} \Omega.m$ is $\sim 10^2$ times (higher), j_c is $\sim 10^{-1}$ - 10^{-2} times (lower), and C_P (for ceramics) is $\sim 10^1$ times (higher), resulting in $\frac{\partial T}{\partial t}$ to be $\sim 10^{-1}$ - 10^{-3} times (lower). This justifies that Joule heating is minimal in the present oxide system.

Discussions:

Combining the stacking fault, suppressed bond-bending and mixed termination at the bottom CMO, the bottom CIO/CMO interface can be inferred to suffer from a combination of three possible suppressions as compared to the top CMO/CIO interface, i.e.: charge transfer fraction, Rashba-type DMI and K_u . Hence the top interface is more privileged to contribute negative-sign AHE, or support magnetic Skyrmion-like bubbles. However, we note that there is no one “smoking-gun” experimental strategy that can unambiguously distinguish the “AHE+THE” and “Bi-AHE” interpretations without controversy. For such thin film heterostructures where separation from substrates is difficult, a highly spin-sensitive scanning-probe tool for Skyrmions imaging such as the nitrogen-vacancy (NV) magnetometry^[51] or scanning nanoSQUID-on-tip^[52] would be invaluable in future work. Nevertheless, proving Skyrmion existence does not invalidate the possibility of two sources of k-space Berry curvatures (for AHE) within the same sample, as shown by the Cr-doped $(Bi_{1-x}Sb_x)_2Te_3$ bilayers case^[27]. These materials may be broadly classified into “systems with strongly spin-textured bands”^[53], which requires more sophisticated theoretical framework and is out-of-scope at present. In conclusion, this work presents the discovery of interesting THE signal evolution at an innovative oxide antiferromagnetic insulator/paramagnetic semimetal interfacial charge-transfer system, suggesting the stabilization of Skyrmion-like magnetic bubbles. This scheme provides an opportunity to access various material combinations across the Periodic Table that may potentially integrate Skyrmion application with antiferromagnetic spintronics, to be unearthed in the near future.

Methods:

By using pulsed laser deposition (PLD) at temperature 680°C and laser fluence 2.5 J/cm², CaMnO₃ and CaIrO₃ films were grown at oxygen ambience of 200 mTorr and 25 mTorr respectively for trilayers, but commonly 75 mTorr for superlattices, followed by cooling at 250 Torr of oxygen to remove oxygen vacancy. Electrical transport and magnetometry were measured in QD Physical Properties Measurement System (PPMS) and Superconducting Quantum Interference Device Vibrating Sample Magnetometer (SQUID-VSM) respectively. Electron Yield XAS was measured at Singapore Synchrotron Light Source (SSLS). Cross sectional High Angle Annular Dark Field (HAADF) and Annular Bright Field (ABF) STEM were performed with a JEOL ARM200F microscope equipped with an ASCOR aberration corrector. Topography scans were done with a Park-Systems NX-10 Atomic Force Microscope (AFM). In Figure 3a, one piece of LAO(001) substrate was cleaved into multiple fragments so as to preserve the same miscut angle and maintain consistency in roughness, while individual layers in a particular sample were grown without breaking vacuum.

Acknowledgements:

This research is supported by the Agency for Science, Technology and Research (A*STAR) under its Advanced Manufacturing and Engineering (AME) Individual Research Grant (IRG) (A1983c0034), the National University of Singapore (NUS) Academic Research Fund (R-144-000-403-114), and the Singapore National Research Foundation (NRF) under the Competitive Research Programs (CRP Award No. NRF-CRP15-2015-01).

Conflict of Interest:

The authors declare no conflicting interest.

References:

- [1] T. Jungwirth, X. Marti, P. Wadley, J. Wunderlich, *Nat. Nanotechnol.* **2016**, *11*, 231; V. Baltz, A. Manchon, M. Tsoi, T. Moriyama, T. Ono, Y. Tserkovnyak, *Rev. Mod. Phys.* **2018**, *90*, 015005.
- [2] P. Wadley, B. Howells, J. Železný, C. Andrews, V. Hills, R. P. Campion, V. Novák, K. Olejník, F. Maccherozzi, S. S. Dhesi, S. Y. Martin, T. Wagner, J. Wunderlich, F. Freimuth, Y. Mokrousov, J. Kuneš, J. S. Chauhan, M. J. Grzybowski, A. W. Rushforth, K. W. Edmonds, B. L. Gallagher, T. Jungwirth, *Science* **2016**, *351*, 587.
- [3] S. S. P. Parkin, M. Hayashi, L. Thomas, *Science* **2008**, *320*, 190; M. Hayashi, L. Thomas, R. Moriya, C. Rettner, S. S. P. Parkin, *Science* **2008**, *320*, 209; S. Parkin, S.-H. Yang, *Nat. Nanotechnol.* **2015**, *10*, 195.
- [4] X. Zhang, Y. Zhou, M. Ezawa, G. P. Zhao, W. Zhao, *Sci. Rep.* **2015**, *5*, 11369; W. Kang, Y. Huang, C. Zheng, W. Lv, N. Lei, Y. Zhang, X. Zhang, Y. Zhou, W. Zhao, *Sci. Rep.* **2016**, *6*, 23164.
- [5] F. Jonietz, S. Mühlbauer, C. Pfleiderer, A. Neubauer, W. Münzer, A. Bauer, T. Adams, R. Georgii, P. Böni, R. A. Duine, K. Everschor, M. Garst, A. Rosch, *Science* **2010**, *330*, 1648; X. Z. Yu, N. Kanazawa, W. Z. Zhang, T. Nagai, T. Hara, K. Kimoto, Y. Matsui, Y. Onose, Y. Tokura, *Nat. Commun.* **2012**, *3*, 988.
- [6] T. Schulz, R. Ritz, A. Bauer, M. Halder, M. Wagner, C. Franz, C. Pfleiderer, K. Everschor, M. Garst, A. Rosch, *Nat. Phys.* **2012**, *8*, 301.
- [7] J. Iwasaki, M. Mochizuki, N. Nagaosa, *Nat. Commun.* **2013**, *4*, 1463.
- [8] S. Finizio, K. Zeissler, S. Wintz, S. Mayr, T. Weßels, A. J. Huxtable, G. Burnell, C. H. Marrows, J. Raabe, *Nano Lett.* **2019**, *19*, 7246.
- [9] N. Romming, C. Hanneken, M. Menzel, J. E. Bickel, B. Wolter, K. von Bergmann, A. Kubetzka, R. Wiesendanger, *Science* **2013**, *341*, 636; P.-J. Hsu, A. Kubetzka, A. Finco, N. Romming, K. von Bergmann, R. Wiesendanger, *Nat. Nanotechnol.* **2016**, *12*, 123.
- [10] W. Jiang, X. Zhang, G. Yu, W. Zhang, X. Wang, M. Benjamin Jungfleisch, John E. Pearson, X. Cheng, O. Heinonen, K. L. Wang, Y. Zhou, A. Hoffmann, Suzanne G. E. te Velthuis, *Nat. Phys.* **2016**, *13*, 162.
- [11] K. Litzius, I. Lemesch, B. Krüger, P. Bassirian, L. Caretta, K. Richter, F. Büttner, K. Sato, O. A. Tretiakov, J. Förster, R. M. Reeve, M. Weigand, I. Bykova, H. Stoll, G. Schütz, G. S. D. Beach, M. Kläui, *Nat. Phys.* **2016**, *13*, 170.
- [12] S. Woo, K. M. Song, X. Zhang, Y. Zhou, M. Ezawa, X. Liu, S. Finizio, J. Raabe, N. J. Lee, S.-I. Kim, S.-Y. Park, Y. Kim, J.-Y. Kim, D. Lee, O. Lee, J. W. Choi, B.-C. Min, H. C. Koo, J. Chang, *Nat. Commun.* **2018**, *9*, 959; L. Caretta, M. Mann, F. Büttner, K. Ueda, B. Pfau, C. M. Günther, P. Helsing, A. Churikova, C. Klose, M. Schneider, D. Engel, C. Marcus, D. Bono, K. Bagschik, S. Eisebitt, G. S. D. Beach, *Nat. Nanotechnol.* **2018**, *13*, 1154.
- [13] X. Zhang, Y. Zhou, M. Ezawa, *Nat. Commun.* **2016**, *7*, 10293; W. Legrand, D. Maccariello, F. Ajejas, S. Collin, A. Vecchiola, K. Bouzehouane, N. Reyren, V. Cros, A. Fert, *Nat. Mater.* **2019**.
- [14] C. Hanneken, F. Otte, A. Kubetzka, B. Dupé, N. Romming, K. von Bergmann, R. Wiesendanger, S. Heinze, *Nat. Nanotechnol.* **2015**, *10*, 1039.
- [15] A. Ohtomo, H. Y. Hwang, *Nature* **2004**, *427*, 423; N. Reyren, S. Thiel, A. D. Caviglia, L. F. Kourkoutis, G. Hammerl, C. Richter, C. W. Schneider, T. Kopp, A.-S. Rüetschi, D. Jaccard, M. Gabay, D. A. Muller, J.-M. Triscone, J. Mannhart, *Science* **2007**, *317*, 1196; L. Li, C. Richter, J. Mannhart, R. C. Ashoori, *Nat. Phys.* **2011**, *7*, 762.
- [16] Z. Zhong, P. Hansmann, *Phys. Rev. X* **2017**, *7*, 011023.
- [17] R. T. Tung, *Applied Physics Reviews* **2014**, *1*, 011304.

- [18] J. Nichols, X. Gao, S. Lee, T. L. Meyer, J. W. Freeland, V. Lauter, D. Yi, J. Liu, D. Haskel, J. R. Petrie, E.-J. Guo, A. Herklotz, D. Lee, T. Z. Ward, G. Eres, M. R. Fitzsimmons, H. N. Lee, *Nat. Commun.* **2016**, *7*, 12721.
- [19] N. Mohanta, E. Dagotto, S. Okamoto, *Phys. Rev. B* **2019**, *100*, 064429.
- [20] J. Ye, Y. B. Kim, A. J. Millis, B. I. Shraiman, P. Majumdar, Z. Tešanović, *Phys. Rev. Lett.* **1999**, *83*, 3737; M. J. Calderón, L. Brey, *Phys. Rev. B* **2001**, *63*, 054421; P. Bruno, V. K. Dugaev, M. Taillefumier, *Phys. Rev. Lett.* **2004**, *93*, 096806; K. Everschor-Sitte, M. Sitte, *J. Appl. Phys.* **2014**, *115*, 172602.
- [21] S. H. Chun, M. B. Salamon, Y. Lyanda-Geller, P. M. Goldbart, P. D. Han, *Phys. Rev. Lett.* **2000**, *84*, 757.
- [22] S. H. Chun, M. B. Salamon, P. D. Han, *Phys. Rev. B* **1999**, *59*, 11155; L. Vistoli, W. Wang, A. Sander, Q. Zhu, B. Casals, R. Cicheler, A. Barthélémy, S. Fusil, G. Herranz, S. Valencia, R. Abrudan, E. Weschke, K. Nakazawa, H. Kohno, J. Santamaria, W. Wu, V. Garcia, M. Bibes, *Nat. Phys.* **2019**, *15*, 67.
- [23] A. Neubauer, C. Pfleiderer, B. Binz, A. Rosch, R. Ritz, P. G. Niklowitz, P. Böni, *Phys. Rev. Lett.* **2009**, *102*, 186602.
- [24] Y. Taguchi, Y. Oohara, H. Yoshizawa, N. Nagaosa, Y. Tokura, *Science* **2001**, *291*, 2573; Y. Machida, S. Nakatsuji, S. Onoda, T. Tayama, T. Sakakibara, *Nature* **2010**, *463*, 210.
- [25] J. Matsuno, N. Ogawa, K. Yasuda, F. Kagawa, W. Koshibae, N. Nagaosa, Y. Tokura, M. Kawasaki, *Sci. Adv.* **2016**, *2*, e1600304; L. Wang, Q. Feng, Y. Kim, R. Kim, K. H. Lee, S. D. Pollard, Y. J. Shin, H. Zhou, W. Peng, D. Lee, W. Meng, H. Yang, J. H. Han, M. Kim, Q. Lu, T. W. Noh, *Nat. Mater.* **2018**, *17*, 1087; K.-Y. Meng, A. S. Ahmed, M. Baćani, A.-O. Mandru, X. Zhao, N. Bagués, B. D. Esser, J. Flores, D. W. McComb, H. J. Hug, F. Yang, *Nano Lett.* **2019**, *19*, 3169.
- [26] W. Wang, M. W. Daniels, Z. Liao, Y. Zhao, J. Wang, G. Koster, G. Rijnders, C.-Z. Chang, D. Xiao, W. Wu, *Nat. Mater.* **2019**, *18*, 1054.
- [27] K. Yasuda, R. Wakatsuki, T. Morimoto, R. Yoshimi, A. Tsukazaki, K. S. Takahashi, M. Ezawa, M. Kawasaki, N. Nagaosa, Y. Tokura, *Nat. Phys.* **2016**, *12*, 555.
- [28] C. Liu, Y. Zang, W. Ruan, Y. Gong, K. He, X. Ma, Q.-K. Xue, Y. Wang, *Phys. Rev. Lett.* **2017**, *119*, 176809; J. Jiang, D. Xiao, F. Wang, J.-H. Shin, D. Andreoli, J. Zhang, R. Xiao, Y.-F. Zhao, M. Kayyalha, L. Zhang, K. Wang, J. Zang, C. Liu, N. Samarth, M. H. W. Chan, C.-Z. Chang, *Nat. Mater.* **2020**.
- [29] S. D. Yi, S. Onoda, N. Nagaosa, J. H. Han, *Phys. Rev. B* **2009**, *80*, 054416.
- [30] D. Kan, T. Moriyama, K. Kobayashi, Y. Shimakawa, *Phys. Rev. B* **2018**, *98*, 180408; D. J. Groenendijk, C. Autieri, T. C. v. Thiel, W. Brzezicki, N. Gauquelin, P. Barone, K. H. W. v. d. Bos, S. v. Aert, J. Verbeeck, A. Filippetti, S. Picozzi, M. Cuoco, A. D. Caviglia, *arXiv* **2018**, arXiv:1810.05619; K. M. Fijalkowski, M. Hartl, M. Winnerlein, P. Mandal, S. Schreyeck, K. Brunner, C. Gould, L. W. Molenkamp, *Phys. Rev. X* **2020**, *10*, 011012.
- [31] S. Satpathy, Z. S. Popović, F. R. Vukajlović, *Phys. Rev. Lett.* **1996**, *76*, 960; J. H. Jung, K. H. Kim, D. J. Eom, T. W. Noh, E. J. Choi, J. Yu, Y. S. Kwon, Y. Chung, *Phys. Rev. B* **1997**, *55*, 15489.
- [32] S. Okamoto, J. Nichols, C. Sohn, S. Y. Kim, T. W. Noh, H. N. Lee, *Nano Lett.* **2017**, *17*, 2126.
- [33] S. Bhowal, S. Satpathy, *Phys. Rev. B* **2019**, *99*, 245145.
- [34] N. Nagaosa, J. Sinova, S. Onoda, A. H. MacDonald, N. P. Ong, *Rev. Mod. Phys.* **2010**, *82*, 1539.
- [35] Y. Zhou, K. Kanoda, T.-K. Ng, *Rev. Mod. Phys.* **2017**, *89*, 025003.
- [36] X. Yu, M. Mostovoy, Y. Tokunaga, W. Zhang, K. Kimoto, Y. Matsui, Y. Kaneko, N. Nagaosa, Y. Tokura, *PNAS* **2012**, *109*, 8856.
- [37] A. Kotani, H. Nakajima, Y. Ishii, K. Harada, S. Mori, **2016**, *6*, 056403; X. Yu, Y. Tokunaga, Y. Taguchi, Y. Tokura, *Adv. Mater.* **2017**, *29*, 1603958.

- [38] N. Nagaosa, Y. Tokura, Nat. Nanotechnol. **2013**, 8, 899; X. Zhang, Y. Zhou, K. Mee Song, T.-E. Park, J. Xia, M. Ezawa, X. Liu, W. Zhao, G. Zhao, S. Woo, J. Phys.: Condens. Matter **2020**, 32, 143001.
- [39] T. Garel, S. Doniach, Phys. Rev. B **1982**, 26, 325; A. O. Leonov, M. Mostovoy, Nat. Commun. **2015**, 6, 8275; S.-Z. Lin, S. Hayami, Phys. Rev. B **2016**, 93, 064430.
- [40] N. F. Mott, in *Physics and Chemistry of Electrons and Ions in Condensed Matter*, (Eds: J. V. Acrivos, N. F. Mott, A. D. Yoffe), Springer Netherlands, Dordrecht 1984, 287.
- [41] S. Bhattacharjee, E. Bousquet, P. Ghosez, J. Phys.: Condens. Matter **2008**, 20, 255229; J. L. Cohn, C. Chiorescu, J. J. Neumeier, Phys. Rev. B **2005**, 72, 024422.
- [42] S. Rohart, A. Thiaville, Phys. Rev. B **2013**, 88, 184422.
- [43] G. A. Jones, Science Progress (1933-) **1976**, 63, 219; A. P. Malozemoff, *Magnetic domain walls in bubble materials*, Academic Press, New York : 1979.
- [44] S. Y. Jang, H. Kim, S. J. Moon, W. S. Choi, B. C. Jeon, J. Yu, T. W. Noh, J. Phys.: Condens. Matter **2010**, 22, 485602; D. Hirai, J. Matsuno, D. Nishio-Hamane, H. Takagi, Appl. Phys. Lett. **2015**, 107, 012104.
- [45] Z. Liao, M. Huijben, Z. Zhong, N. Gauquelin, S. Macke, R. J. Green, S. Van Aert, J. Verbeeck, G. Van Tendeloo, K. Held, G. A. Sawatzky, G. Koster, G. Rijnders, Nat. Mater. **2016**, 15, 425.
- [46] A. Marthinsen, C. Faber, U. Aschauer, N. A. Spaldin, S. M. Selbach, MRS Communications **2016**, 6, 182.
- [47] J. Kanamori, J. Phys. Chem. Solids **1959**, 10, 87.
- [48] A. A. Thiele, Phys. Rev. Lett. **1973**, 30, 230.
- [49] J. Zang, M. Mostovoy, J. H. Han, N. Nagaosa, Phys. Rev. Lett. **2011**, 107, 136804.
- [50] S.-Z. Lin, C. Reichhardt, C. D. Batista, A. Saxena, Phys. Rev. B **2013**, 87, 214419.
- [51] Y. Dovzhenko, F. Casola, S. Schlotter, T. X. Zhou, F. Büttner, R. L. Walsworth, G. S. D. Beach, A. Yacoby, Nat. Commun. **2018**, 9, 2712.
- [52] D. Vasyukov, Y. Anahory, L. Embon, D. Halbertal, J. Cuppens, L. Neeman, A. Finkler, Y. Segev, Y. Myasoedov, M. L. Rappaport, M. E. Huber, E. Zeldov, Nat. Nanotechnol. **2013**, 8, 639.
- [53] Z. Liao, P. Jiang, Z. Zhong, R.-W. Li, npj Quantum Materials **2020**, 5, 30.

Figures:

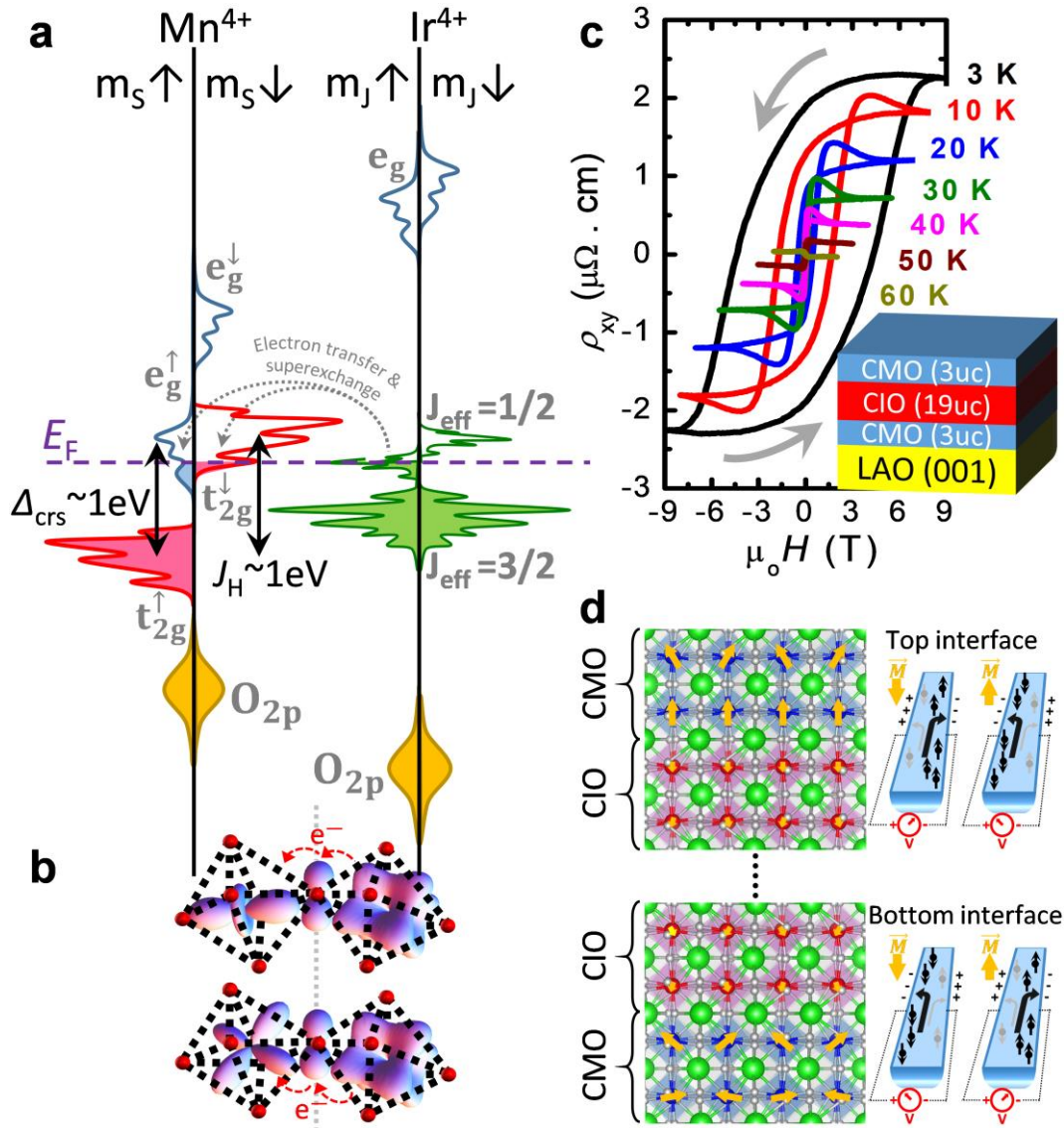


Figure 1. (a) Fundamental magnetic properties and Hall data in $\text{Ca-Mb}_3\text{I}_9\text{Mt}_3$. Sketch of single-ion DOS of Mn^{4+} and Ir^{4+} in perovskite B-site after contact and magnetic superexchange. Before contact, O_{2p} bands are aligned but E_F are misaligned (not shown). **(b)** Orbital sketches illustrating the two possible transfer paths in an octahedral-tilted perovskite environment. **(c)** Hall data obtained from the $\text{Ca-Mb}_3\text{I}_9\text{Mt}_3$ structure. **(d)** Left: a sketch illustrating the possible Mn and Ir moments alignment (yellow arrows) at the top and bottom interfaces respectively. Right: the corresponding AHE mechanisms that support the “Bi-AHE” interpretation.

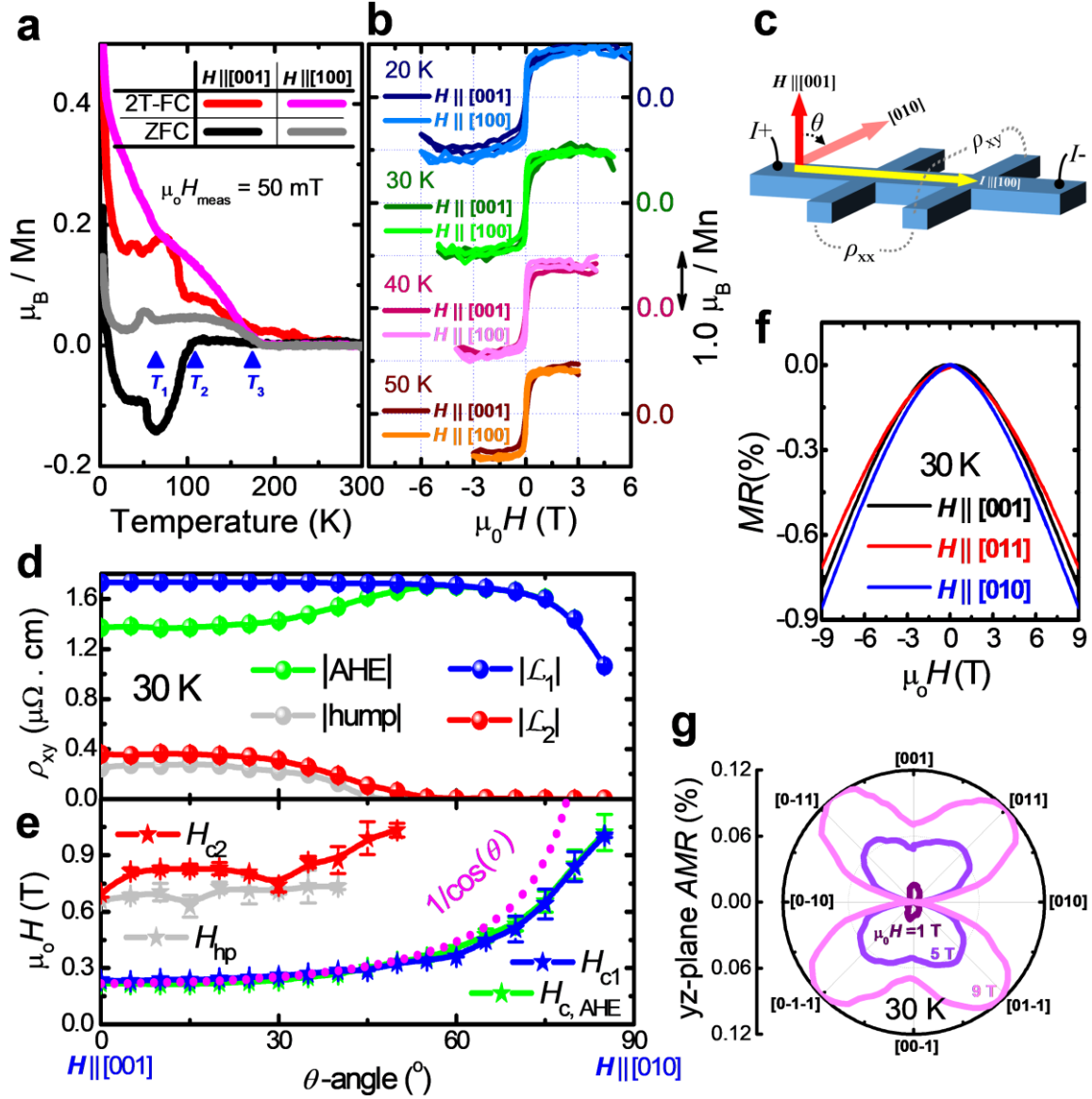


Figure 2. Magnetometry and anisotropic magneto-transport of $\text{Ca-Mb}_3\text{I}_9\text{Mt}_3$. (a) 2 T-field-cooled (FC) and zero-field-cooled (ZFC) $M-T$ and (b) $M-H$ curves with data shifted vertically for clarity. (c) Schematic of θ -dependent Hall measurement. (d) θ -dependence of extraordinary Hall Effect decomposed into respective components following the two debated interpretations. (e) θ -dependence of $H_{c, \text{AHE}}$, H_{hp} and $H_{c1,2}$. The dotted line shows the expected $1/\cos(\theta)$ trend. (f) $MR(H) = \frac{R_{xx}(H) - R_{xx}(H=0)}{R_{xx}(H=0)} \times 100\%$ for various magnetic field directions. (g) $AMR(\theta) = \frac{R_{xx}(\theta) - R_{xx}(H \parallel [010])}{R_{xx}(H \parallel [010])} \times 100\%$ at various fields.

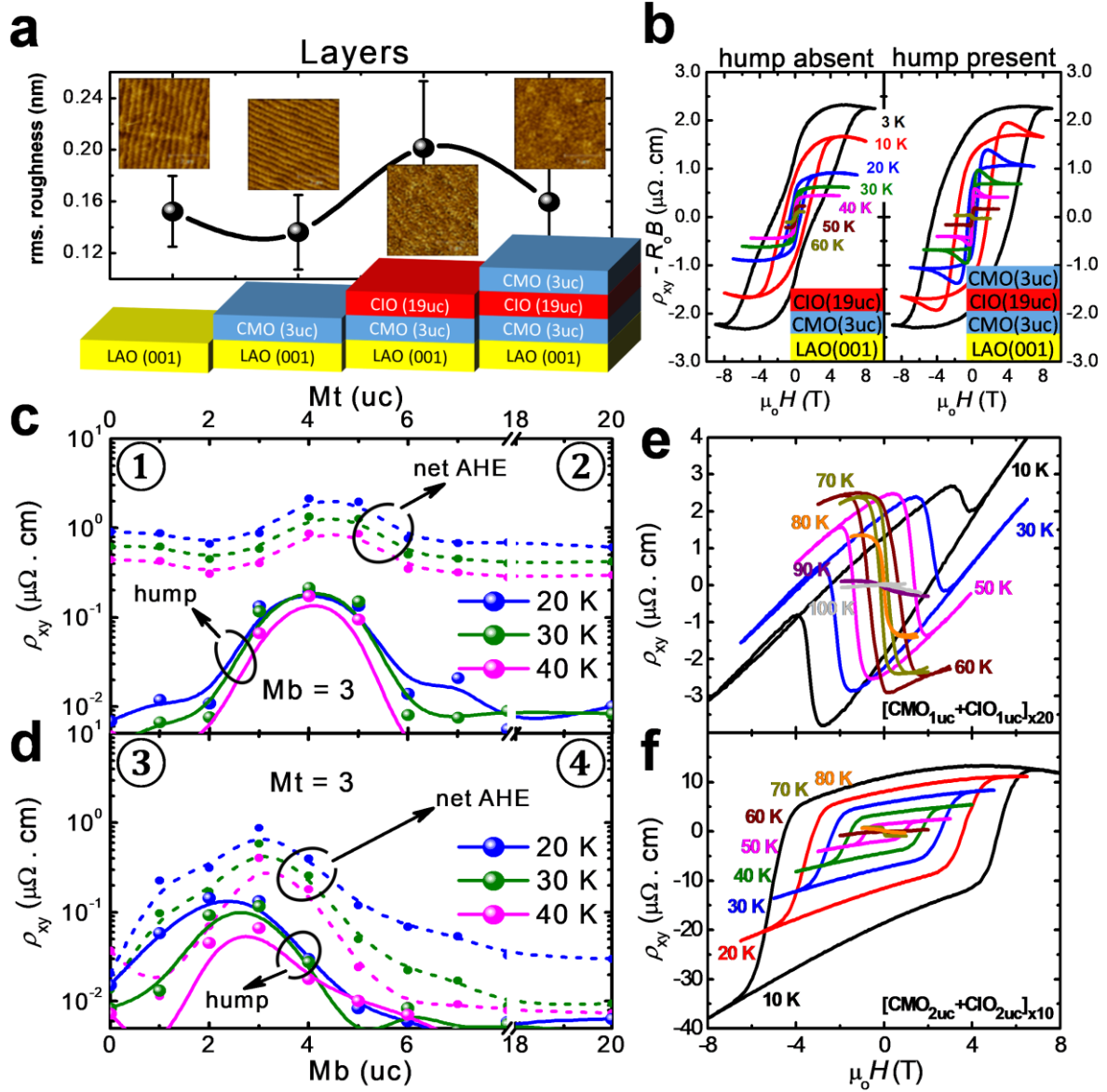


Figure 3. Tuning the layer thickness of trilayer and superlattices. (a) Layer-dependent surface roughness with topography attached. (b) Comparison between the Hall Effect of $\text{Ca-Mb}_3\text{I}_{19}\text{Mt}_0$ and $\text{Ca-Mb}_3\text{I}_{19}\text{Mt}_3$. Hall Effect variation by tuning the (c) top and (d) bottom CMO thickness of $\text{Ca-Mb}_3\text{I}_{19}\text{Mt}_3$. Hall Effect of (e) [m=1]-SL and (f) [m=2]-SL showing opposite-sign AHE loops.

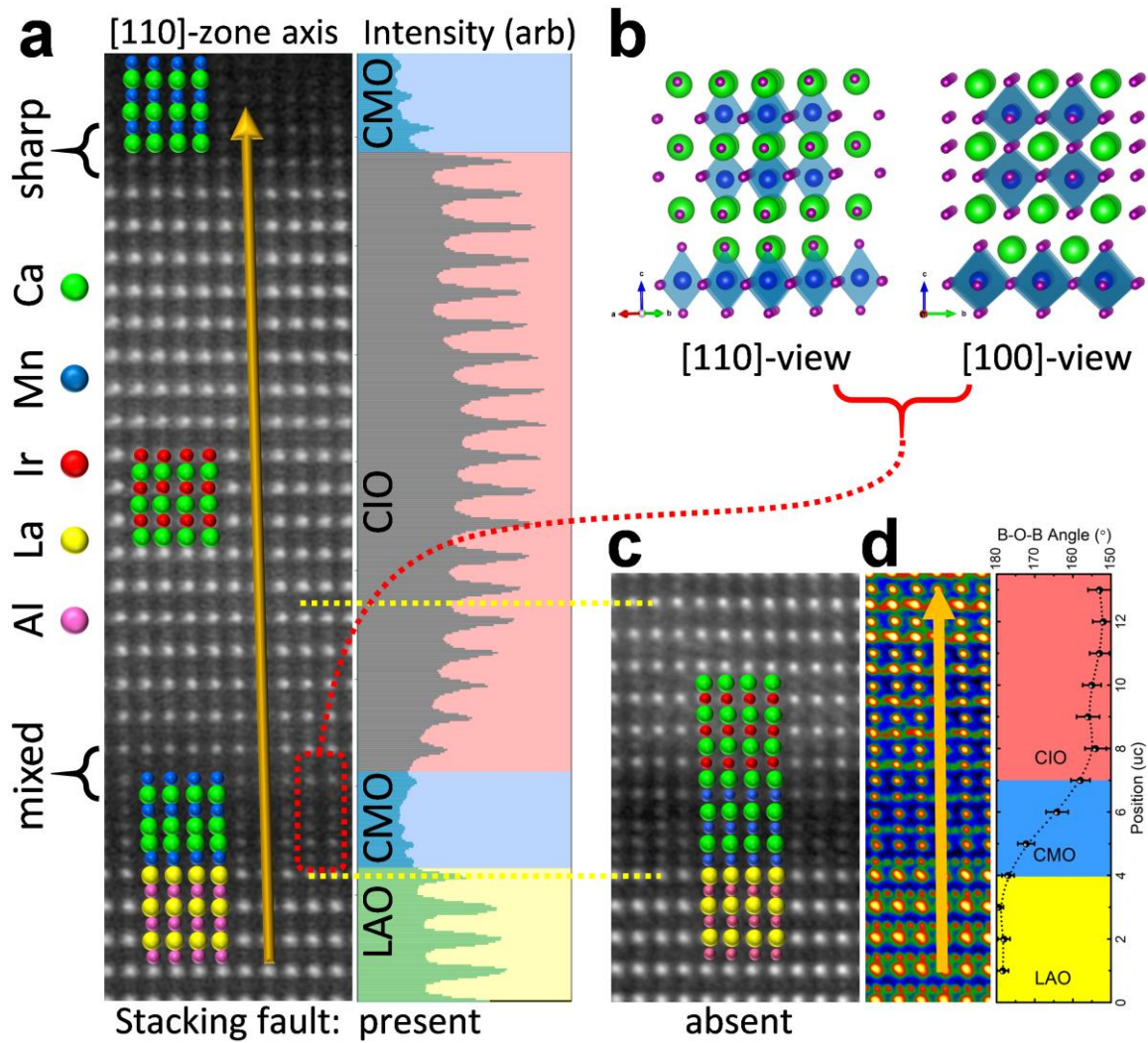


Figure 4. STEM study on $\text{Ca-Mb}_3\text{I}_9\text{Mt}_3$ along $[110]$ -zone axis. (a) High-angle Annular Dark-field (HAADF) image (left) with element-specific intensity (right). The bracketed region is identified with a stacking fault that can be understood in (b), while ‘mixed’ refers to termination. (c) Image of another region of the same sample similar to (a) but without stacking fault. (d) B-O-B bond angle plotted with distance (right panel), extracted from an Annular Bright-field (ABF) image (left panel). Ir-O-Ir bond angles at higher position are not provided due to difficulty in analyzing blurry image. Brown arrows in (a), (d) indicate the selected atoms for intensity and bond angle analyses.

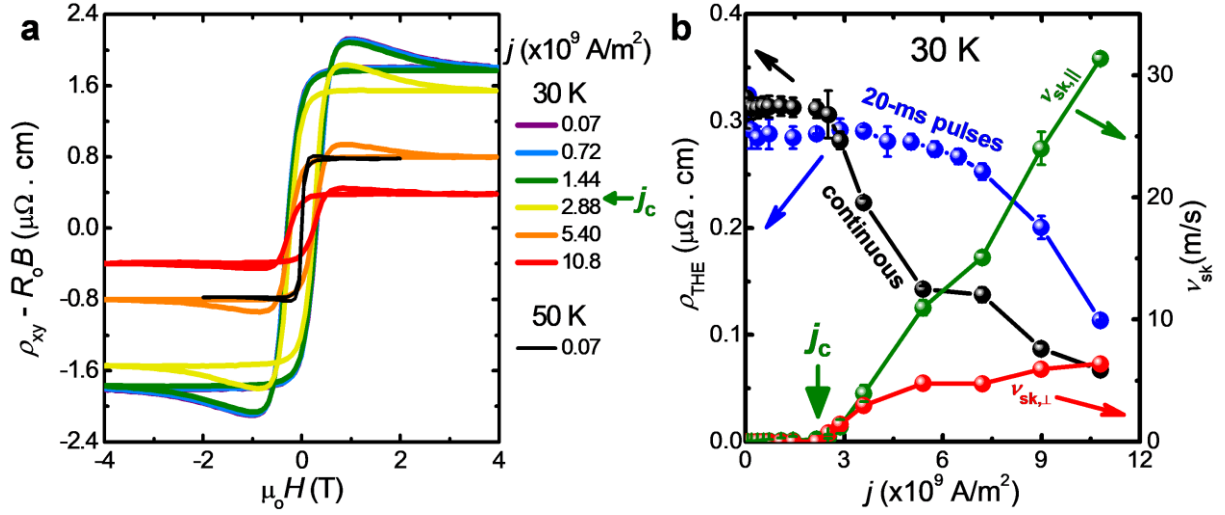


Figure 5. Current-driven dynamics of magnetic bubbles. (a) Hall Effect loops with various current densities at 30 K. The 50 K loop at low current with very narrow H_c is shown for comparison to indicate the irrelevance of Joule heating. (b) Peak THE (hump signal) variations with increasing current density, under the “continuous” (extracted from (a)) and “20 ms-pulse” current modes. Estimated Skyrmion velocity components from the “continuous” mode curve are plotted together.

Supporting Information

Topological Hall Effect and Skyrmion-like Bubbles at a Charge-transfer Interface

*Zhi Shiuh Lim, Changjian Li, Zhen Huang, Xiao Chi, Jun Zhou, Shengwei Zeng, Ganesh Ji Omar, Yuan Ping Feng, Andrivo Rusydi, Stephen John Pennycook, Thirumalai Venkatesan, Ariando**

Dr. Z. S. Lim, Dr. C. Li, Dr. Z. Huang, Dr. S.W. Zeng, G. J. Omar, Prof. T. Venkatesan, Prof. Ariando

NUSNNI-NanoCore, National University of Singapore, Singapore 117411

email: phyarian@nus.edu.sg

Dr. Z. S. Lim, Dr. Z. Huang, Dr. X. Chi, Dr. J. Zhou, Dr. S.W. Zeng, G. J. Omar, Prof. T. Venkatesan, Prof. A. Rusydi, Prof. Ariando

Department of Physics, National University of Singapore, Singapore 117542

Dr. X. Chi, Prof. A. Rusydi

Singapore Synchrotron Light Source (SSLS), National University of Singapore, 5 Research Link, Singapore 117603

Dr. C. Li, Prof. S. J. Pennycook, Prof. T. Venkatesan,

Department of Materials Science and Engineering, National University of Singapore, Singapore 119077

1. Bi-AHE fittings for the θ -dependent Hall Effect Analyses

Figure S1a shows the θ -dependent extraordinary Hall data and their decomposition into humps and (net) AHE following the “AHE+hump” scheme, or into $\mathcal{L}_{1,2}(H)$ following the “Bi-AHE” scheme. The “AHE+hump” fitting is straightforward. The net AHE component is the data up to saturation at large field, and the remaining antisymmetric hump signal, which decays to zero at large field, is obtained by subtracting the net AHE away from the original data. On the other hand, the $\mathcal{L}_{1,2}(H)$ fitting could be arbitrary due to information loss. To assume a reasonable guideline, we assign the AHE loop at $\theta=60^\circ$, which appears to be the highest and without humps, as the maximum \mathcal{L}_1 . This way, \mathcal{L}_2 exists up to $\theta\sim 60^\circ$ and can be obtained by subtracting \mathcal{L}_1 away from the original data. At $\theta>60^\circ$, \mathcal{L}_2 is zero and not shown.

2. Further discussions on anisotropic magnetoresistance (AMR) measurements

In main text Figure 2f-g, we see a fourfold symmetry with θ -rotation, where the [001] out-of-plane direction could be interpreted as the easy-axis of the ferromagnetic top CMO/CIO interface due to adequate charge transfer; while the [010] in-plane direction could be the easy-axis of the canted antiferromagnetic bottom CIO/CMO interface due to low charge transfer. This way, the [011] is naturally the hard-axis. Note that the measurement configuration (yz-plane θ -rotation) in main text Figure 2c eliminates the SOC-assisted s-d scattering mechanism^[1] in AMR, but does not eliminate the Spin Hall Magnetoresistance (SMR)^[2]. However, from Ref. [3], the two schemes of out-of-plane to in-plane magnetic field rotation (yz-plane θ -rotation) and (xz-plane γ -rotation) usually yield the same result, suggesting that both the SOC-assisted s-d scattering and SMR are negligible compared to magnetic anisotropy in our system.

3. CIO thickness variation in CMO/CIO/CMO trilayer

Following the two-carrier model for a compensated semimetal which is a good description for CaIrO_3 , the ordinary Hall Effect (OHE) collapses into a simpler linear form^[4], hence $R_0 =$

$\left. \frac{\partial \rho_{xy}}{\partial B} \right|_{B \rightarrow \infty} = \frac{1}{en} \left(\frac{\mu_h - \mu_e}{\mu_h + \mu_e} \right)$. As shown in **Figure S1b-c**, it is obvious that the magnitudes of net

AHE increase with the sign-reversal of R_o , although the trend of hump is less obvious. Logically, we expect the part of CIO away from interfaces remain near compensated (bulk-like) but the interfacial CIO within its Thomas-Fermi screening length is significantly hole-doped due to the charge transfer. Hence, at the interface, the holes would dominate over electrons and mainly contributes the AHE signal, and μ_e could be neglected. Yet, in actual measurement of the trilayer, both the mentioned parts are measured together, forming the total R_o by a simple summation of Hall resistivity and linear conductivity (in parallel circuit) from

both parts. Hence, $R_o = \frac{f}{en_{sm}} \left(\frac{\mu_{h,sm} - \mu_{e,sm}}{\mu_{h,sm} + \mu_{e,sm}} \right) + \frac{(1-f)}{en_{hd}}$, and $\sigma_{xx}(B=0) = f n_{sm} e (\mu_{h,sm} + \mu_{e,sm}) + (1-f) n_{hd} \mu_{hd} e$, where subscript “sm” and “hd” denote “semimetallic” and “hole-doped” respectively, and f is the fraction proportional to the CIO’s thickness. We can expect $\mu_{e,sm} > \mu_{h,sm}$ due to the slightly lighter electron’s effective mass. This way, the first term of R_o is a negative constant, and R_o sign-reversal occurs following the increasing CIO thickness. Yet, it is reasonable to assume that AHE is only contributed by the interface, hence, the linear scaling relationship seen in Figure S1c is simply reduced to $\rho_{AHE} \propto R_{o,hd} = \frac{C}{en_{hd}}$ (neglecting the semimetallic part), and the relevant $\rho_{xx}(B=0) = \frac{1}{n_{hd} \mu_{hd} e}$. This way, $\sigma_{AHE} =$

$$\frac{\rho_{AHE}}{\rho_{AHE}^2 + \rho_{xx}^2(B=0)} \approx \frac{\frac{C}{en_{hd}}}{\left(\frac{C}{en_{hd}} \right)^2 + \left(\frac{1}{n_{hd} \mu_{hd} e} \right)^2} = \frac{en_{hd} k \mu_{hd}^2}{\mu_{hd}^2 C^2 + 1}. \text{ Here, it is straightforward that } C \text{ has the}$$

dimension of magnetic field and is ~ 4 T at 20 K, ~ 3 T at 30 K, and ~ 2 T at 40 K. From the supplementary data of Ref. [3], we see that the carrier mobilities are no more than $5 \times 10^{-3} \text{ m}^2/\text{V/s}$ at these temperatures, hence $\mu_{hd}^2 C^2 \ll 1$. This would place our system approximately in the category of bad metal hopping “dirty limit” ($\sigma_{AHE} \sim \mu_{hd}^{1.6} \sim \sigma_{xx}^{1.6}$) with coexistence of both intrinsic and side-jump mechanisms^[5]. While the opposite regime $\mu_{hd}^2 C^2 \gg 1$ corresponding to the moderately dirty limit ($\sigma_{AHE} \sim \mu_{hd}^0$) is not applicable here. The fast

exponential increase of $\rho_{\text{THE}} \propto n^{-8/3}$ as observed in lightly-doped $\text{Ce}_x\text{Ca}_{1-x}\text{MnO}_3$ thin films^[6], which is the Topological Hall Effect (THE) in the weak coupling regime enhanced by strong correlation and increase in electron's effective mass with reducing Ce^{4+} -doping, is also not observed here.

4. Analyses of X-ray Absorption (XAS) spectra

The Mn $L_{2,3}$ -edge and O K-edge XAS spectra of pure CaMnO_3 film and superlattices at 300 K are shown in **Figure S2a-b**. First, comparing Mn $L_{2,3}$ -edges (Figure S2a, inset) which are excitations from the Mn2p_{1/2} and 2p_{3/2} core levels to the empty Mn3d valence states, a gradual redshift of peaks can be observed in the sequence from CaMnO_3 , [m=2]-SL to [m=1]-SL. This indicates that their Mn2p core level electrons have reducing binding energy, implying a gradual reduction of oxidation state of the Mn-species, verifying the charge transfer from Ir^{4+} to Mn^{4+} .

Next, we analyse the O K-edge spectra (Figure S2b) for bulk-like CaMnO_3 , CaIrO_3 , [m=1] and [m=2] CMO-CIO superlattices, which are excitations from the O1s core level to the empty O2p-Mn3d and O2p-Ir5d hybridized states. We should note: Mn^{4+} is Jahn-Teller inactive and the fully-filled Mn3d t_{2g}^{\uparrow} orbitals do not contribute any O K edge signal. Hence, the peaks are labelled in the table below:

Ⓐ	$\text{O}1s \rightarrow \text{O}2p\text{-Mn}3d\ e_g^{\uparrow}$			
Ⓑ	$\text{O}1s \rightarrow \text{O}2p\text{-Mn}3d\ t_{2g}^{\downarrow}$		Ⓐ	$\text{O}1s \rightarrow \text{O}2p\text{-Ir}5d\ t_{2g}^{\text{J}_{\text{eff}}=1/2}$
Ⓒ	$\text{O}1s \rightarrow \text{O}2p\text{-Mn}3d\ e_g^{\downarrow}$		Ⓑ	$\text{O}1s \rightarrow \text{O}2p\text{-Ir}5d\ e_g$
Ⓓ,Ⓔ	$\text{O}1s \rightarrow \text{O}2p\text{-Ca}4d$		Ⓒ	$\text{O}1s \rightarrow \text{O}2p\text{-Ca}4d$

Ⓕ,Ⓖ,Ⓗ	O1s → O2p-Mn4s/4p	Ⓓ	O1s → O2p-Ir6s/6p
-------	-------------------	---	-------------------

The near-overlapping peaks Ⓐ and Ⓑ^[7, 8] play the key role of stabilizing AHE sign-reversal discussed in this paper. This feature of CaMnO₃ is not to be confused with that of LaMnO₃ where peaks Ⓐ and Ⓒ are split, since Mn³⁺ with half-filling of the e_g[↑] band is Jahn-Teller active, and peak Ⓑ is also pushed further up energetically due to increased Hund's coupling (J_H)^[7, 9]. Peaks Ⓓ, Ⓔ, Ⓕ, Ⓖ, Ⓗ, Ⓒ, and Ⓓ will not be subjected to further analyses. Comparing between CMO, [m=2]-SL and [m=1]-SL, we see reducing peak height at Ⓑ due to increasing occupancy (less empty) at Mn3d t_{2g}[↓], evidencing charge transfer.

5. Magnetometry for superlattices

Magnetization-temperature (M-T) curves in **Figure S2c-d** show that there is a distinct T_{C1} at ~100 K (for [m=1]-SL and ~80 K for [m=2]-SL, below which Mn^{(4-δ)+} moments order ferromagnetically. Above T_{C1}, the “spin-nematic/liquid” order of Ir^{(4+δ)+} persists up to >300 K. Perpendicular magnetic anisotropy (PMA) exists in both superlattices. The higher T_{C1} of [m=1]-SL than [m=2]-SL also proves its higher percentage of charge transfer, similar to J. Nichols' result^[10]. Since the CIO spacers in the superlattices are thin, the magnetic moments are fully coupled, sharing the same coercive field, hence no hump signal is observable in the Hall Effect of these superlattices (main text Figure 3e-f) although small cancellation may exist.

6. Computational techniques

First-principle calculations were done by Density Functional Theory (DFT) based on the Vienna *Ab-initio* Simulation Package (VASP)^[11] with the Local-density Approximation (LDA) for the exchange-correlation functional^[12] and the frozen-core all-electron projector-augmented wave (PAW) method^[13] for the electron-ion interaction. Mott-Hubbard interaction (U) and Spin-orbit Coupling (SOC) are added to improve accuracy of results, specifically U =

2 eV for Ir-site^[14] and $U = 5$ eV for Mn-site^[15]. The cutoff energy for the plane wave expansion was set to 520 eV. For all present cases, a $6 \times 6 \times 3$ k-point grid for Brillouin zone sampling is found to be sufficient. All the atoms are allowed to relax until the forces were smaller than 0.01 eV/Å.

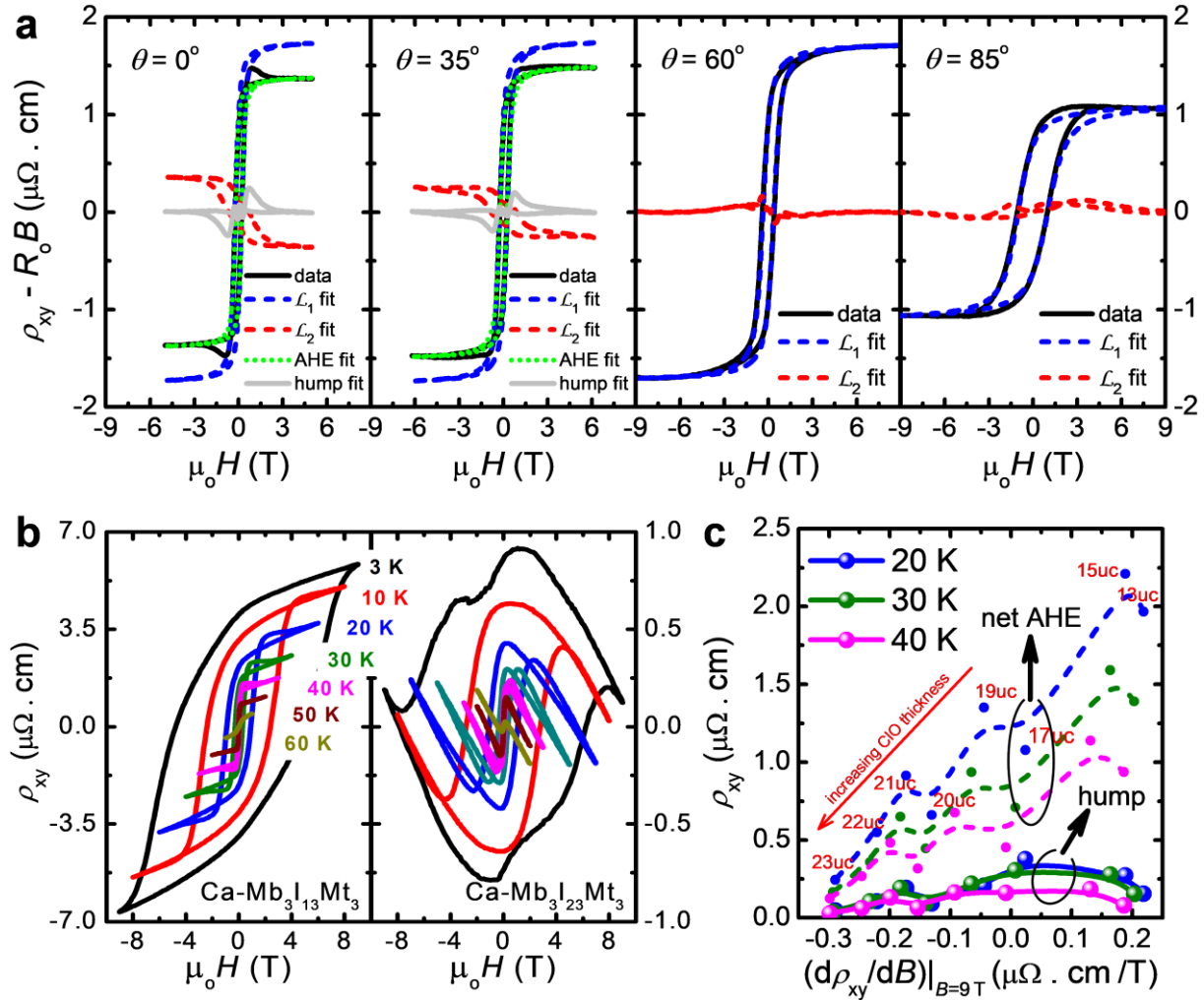
The calculated band structures, lattice parameters and Bader charges of bulk perovskite CaIrO_3 and CaMnO_3 are shown in **Figure S3**, agreeing with earlier publications. The metastable perovskite CaIrO_3 polymorph is calculated by LDA-PAW+U+SOC yielding a paramagnetic semimetal ground state^[14], this is not to be confused to the more stable post-perovskite CaIrO_3 structure which is a spin-orbit Mott insulator^[16]. Whereas CaMnO_3 is calculated by LDA-PAW+U yielding a G-type antiferromagnetic Mott insulator ground state with Ising-like $\pm 2.712 \mu_B/\text{Mn}$, and an indirect bandgap of 1.46 eV^[15, 17].

A supercell of $[\text{CaIrO}_3 (2\text{uc})/\text{CaMnO}_3 (2\text{uc})]_{\infty}$ superlattice is built using 4 Mn, 4 Ir, 8 Ca and 24 O atoms, and the equilibrium atom positions and bond angles after relaxation are shown in **Figure S4a**. In the superlattice, all Mn moments are enhanced compared to the bulk CaMnO_3 , while Mn and Ir moments are antiparallel and pointing towards the $\langle 111 \rangle$ axis. In the orbital-resolved density-of-states (DOS) plotted in **Figure S4b**, e_g orbitals have large DOS at Fermi level (E_F). Comparing the Bader charges (**Figure S3f, S4c**) of Mn representing the number of electrons in the 3rd atomic valence shell ($\sim 3s^2 3p^6 3d^3$), there is an increase of 0.11 from the bulk CaMnO_3 to the Ca- M_2I_2 -SL, implying that the charge transfer from Ir to Mn is around $0.11e^-$. This is less than that of (extrapolated) $[\text{SrMnO}_3 (2\text{uc})/\text{SrIrO}_3 (2\text{uc})]_{\text{xn}}$ superlattice reported in Ref. ^[10] ($\sim 0.35e^-$), probably due to larger octahedral tilt (smaller Mn-O-Ir bond angle) in the present work with smaller Ca^{2+} at the A-site compared to Sr^{2+} . Nevertheless, ferromagnetic coupling between Mn moment still exists since it fulfills the critical charge transfer fraction $x_c \sim 0.11$ according to Bhowal's result^[18].

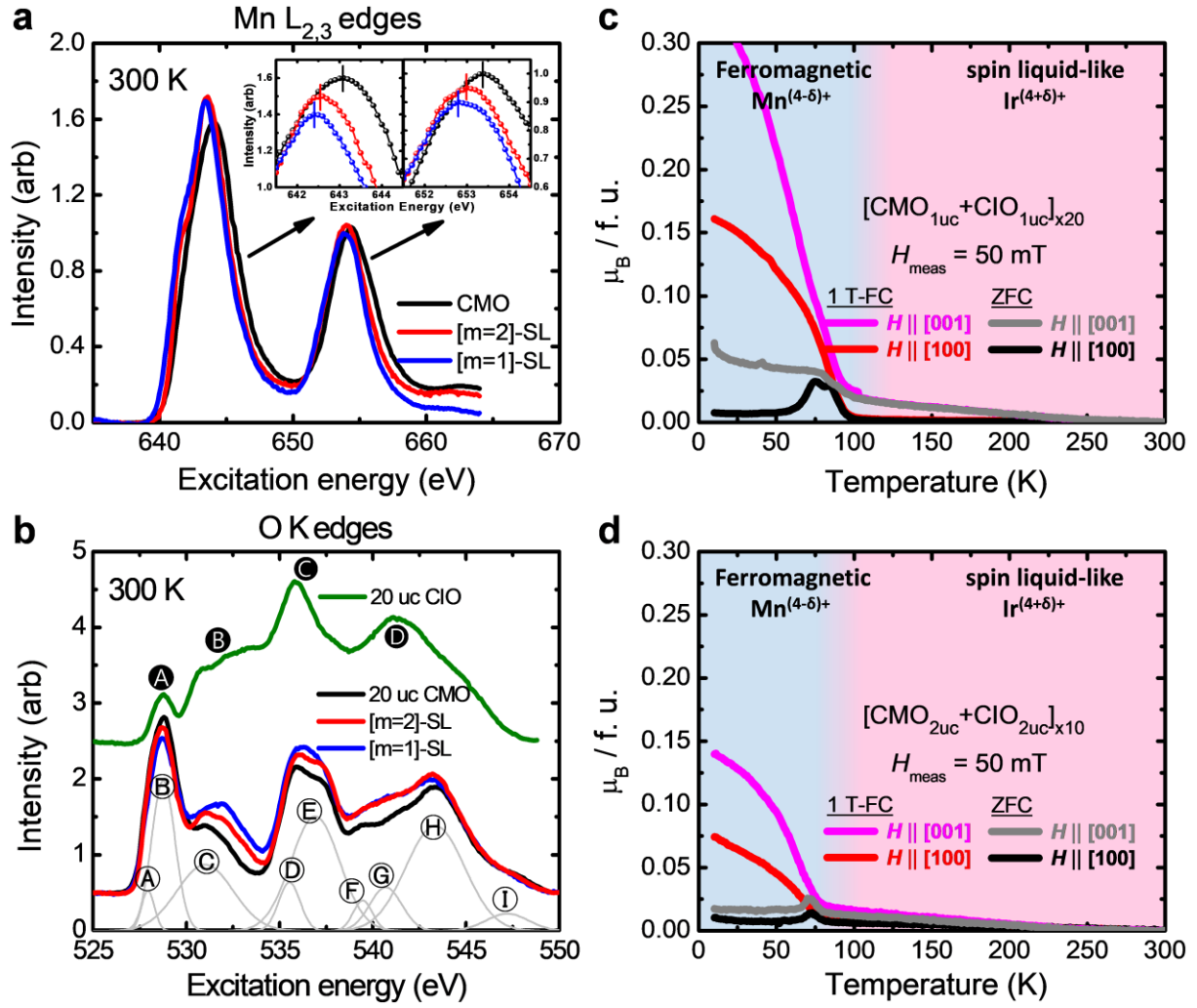
Supporting References:

- [1] R. C. O'Handley, *Modern magnetic materials: principles and applications*, Wiley, New York 1999.
- [2] H. Nakayama, M. Althammer, Y. T. Chen, K. Uchida, Y. Kajiwara, D. Kikuchi, T. Ohtani, S. Geprägs, M. Opel, S. Takahashi, R. Gross, G. E. W. Bauer, S. T. B. Goennenwein, E. Saitoh, *Phys. Rev. Lett.* **2013**, *110*, 206601.
- [3] Z. S. Lim, C. Li, X. Chi, G. J. Omar, H. H. Ma, Z. Huang, S. Zeng, P. Yang, T. Venkatesan, A. Rusydi, S. J. Pennycook, A. Ariando, *Nano Lett.* **2020**, *20*, 1890.
- [4] M. D. Watson, T. Yamashita, S. Kasahara, W. Knafo, M. Nardone, J. Béard, F. Hardy, A. McCollam, A. Narayanan, S. F. Blake, T. Wolf, A. A. Haghighirad, C. Meingast, A. J. Schofield, H. v. Löhneysen, Y. Matsuda, A. I. Coldea, T. Shibauchi, *Phys. Rev. Lett.* **2015**, *115*, 027006.
- [5] N. Nagaosa, J. Sinova, S. Onoda, A. H. MacDonald, N. P. Ong, *Rev. Mod. Phys.* **2010**, *82*, 1539.
- [6] L. Vistoli, W. Wang, A. Sander, Q. Zhu, B. Casals, R. Cichelero, A. Barthélémy, S. Fusil, G. Herranz, S. Valencia, R. Abrudan, E. Weschke, K. Nakazawa, H. Kohno, J. Santamaria, W. Wu, V. Garcia, M. Bibes, *Nat. Phys.* **2019**, *15*, 67; K. Nakazawa, M. Bibes, H. Kohno, *J. Phys. Soc. Jpn.* **2018**, *87*, 033705.
- [7] J. H. Jung, K. H. Kim, D. J. Eom, T. W. Noh, E. J. Choi, J. Yu, Y. S. Kwon, Y. Chung, *Phys. Rev. B* **1997**, *55*, 15489.
- [8] S. Satpathy, Z. S. Popović, F. R. Vukajlović, *Phys. Rev. Lett.* **1996**, *76*, 960; C.-J. Liu, A. Bhaskar, J. J. Yuan, Z.-R. Yang, S.-S. Chen, H.-C. Chen, F.-W. Liao, Yu T. Lin, Ping H. Yeh, C.-Y. Lai, C.-L. Chang, *Ceram. Int.* **2016**, *42*, 4048.
- [9] G. Subías, J. García, M. C. Sánchez, J. Blasco, M. G. Proietti, *Surf. Rev. Lett.* **2002**, *09*, 1071.
- [10] J. Nichols, X. Gao, S. Lee, T. L. Meyer, J. W. Freeland, V. Lauter, D. Yi, J. Liu, D. Haskel, J. R. Petrie, E.-J. Guo, A. Herklotz, D. Lee, T. Z. Ward, G. Eres, M. R. Fitzsimmons, H. N. Lee, *Nat. Commun.* **2016**, *7*, 12721.
- [11] G. Kresse, J. Hafner, *Phys. Rev. B* **1994**, *49*, 14251; G. Kresse, J. Non-Cryst. Solids **1995**, *192-193*, 222.
- [12] J. P. Perdew, A. Zunger, *Phys. Rev. B* **1981**, *23*, 5048.
- [13] P. E. Blöchl, *Phys. Rev. B* **1994**, *50*, 17953.
- [14] S. Y. Jang, H. Kim, S. J. Moon, W. S. Choi, B. C. Jeon, J. Yu, T. W. Noh, *J. Phys.: Condens. Matter* **2010**, *22*, 485602.
- [15] M. Molinari, D. A. Tompsett, S. C. Parker, F. Azough, R. Freer, *Journal of Materials Chemistry A* **2014**, *2*, 14109.
- [16] M. M. Sala, K. Ohgushi, A. Al-Zein, Y. Hirata, G. Monaco, M. Krisch, *Phys. Rev. Lett.* **2014**, *112*, 176402.
- [17] E. O. Wollan, W. C. Koehler, *Phys. Rev.* **1955**, *100*, 545.
- [18] S. Bhowal, S. Satpathy, *Phys. Rev. B* **2019**, *99*, 245145.

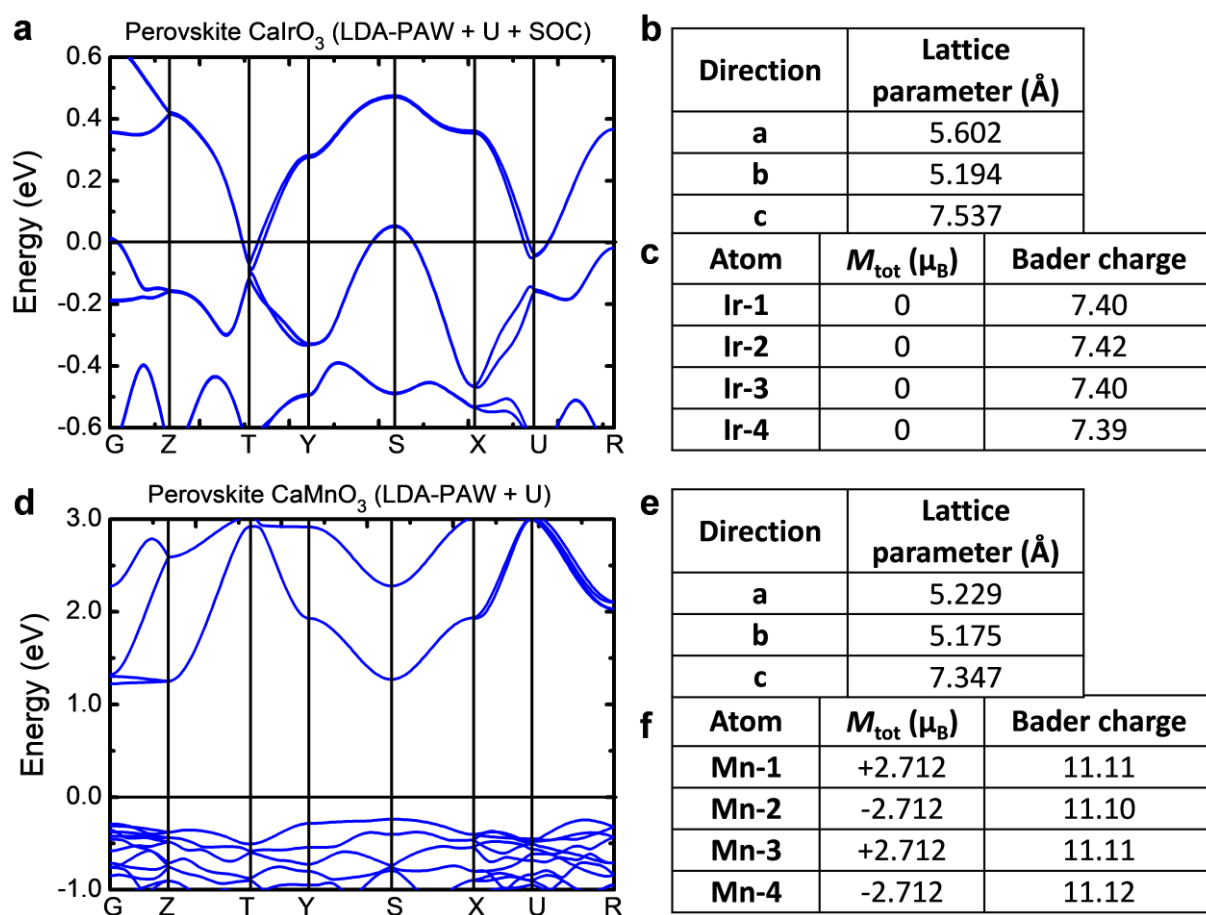
Supporting Figures:



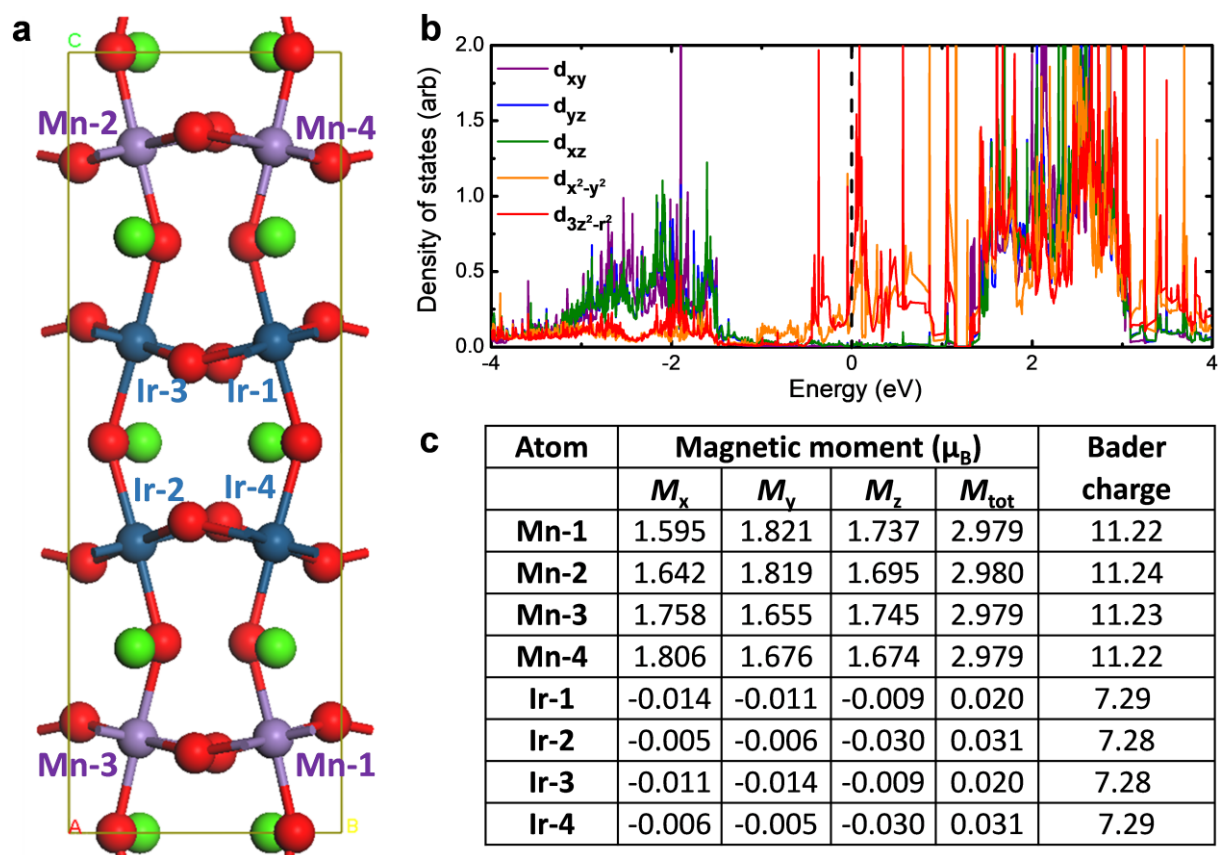
Supporting Figure S1. (a) Deconvolution of Extraordinary Hall Effect data into various components following the "AHE+hump" and "Bi-AHE" interpretations, measured at increasing θ -angle away from out-of-plane magnetic field. (b) Hall Effect (inclusive of the Ordinary Hall (OHE) component from Lorentz force) of the trilayer structure with different CIO spacer thicknesses. Note the OHE gradient sign-reversal accompanies the reduction of overall abscissa scale (right side), although the hump signal is present in both structures. (c) A summary of Extraordinary Hall Effect evolution presented in the "AHE+hump" format, with the tuning of CIO layer thickness and fixed CMO thickness at $\text{Mt}=\text{Mb}=3\text{uc}$.



Supporting Figure S2. XAS spectra for (a) Mn $L_{2,3}$ edges and (b) O K edges of the thick $CaMnO_3$ film and [m=1,2]-SLs grown on LAO(001) with fitting peaks labelled ① to ⑩. In (b), the O K edges of thick CIO//LAO(001) is also shown for comparison. The baselines of the CIO, CMO and superlattices are shifted vertically away from the fitting peaks for clarity. M-T curves measured with in-plane and out-of-plane fields for the (c) [m=1]-SL and (d) [m=2]-SL.



Supporting Figure S3. DFT calculations result for the bulk CaIrO_3 and CaMnO_3 . **(a,d)** The E-k band diagrams of CaIrO_3 (a) and CaMnO_3 (d). **(b,e)** Orthorhombic lattice parameters for CaIrO_3 (b) and CaMnO_3 (e). **(c,f)** Moments and Bader charges for neighboring Ir (c) and Mn (f) species. The +/- signs for CaMnO_3 indicates G-type antiferromagnetic.



Supporting Figure S4. DFT calculations for the $[\text{CaIrO}_3(2\text{uc})/\text{CaMnO}_3(2\text{uc})]_{\infty}$ superlattice.

(a) One unit supercell after relaxation. (b) Orbital-resolved DOS, with $E_F = 0$ eV (dashed line).

(c) Moments and Bader charges for the Mn and Ir species, with the atoms labeled referring to (a).